Nanoscale Advances

ROYAL SOCIETY OF CHEMISTRY

PAPER

View Article Online
View Journal | View Issue

Cite this: *Nanoscale Adv.*, 2025, **7**, 8074

Ethylenediamine modified carbon nanospheres from biomass for selective membrane filtration

B. G. Maya Patel,[ab] Sk Safikul Islam,[c] Samir Mandal,[d] Suryasarathi Bose [d] and Gurumurthy Hegde *[ab]

The present work investigates the antifouling properties dye and antibiotic removal efficiency of PVDF/E-CNS membranes. Carbon nanospheres (CNS) derived from rice husk (RH) were pyrolyzed at 800 °C. Further, ethylenediamine functionalized carbon nanospheres (E-CNS) were obtained *via in situ* decoration of ethylenediamine on acid-functionalized carbon nanospheres (O-CNS). The synthesized E-CNS were characterized by techniques such as XRD, FESEM, Raman spectroscopy, FTIR and BET. The membranes were fabricated by integrating E-CNS at varying loadings (0.1–0.7 wt%) *via* a non-solvent induced phase separation (NIPS) technique. The membrane properties were assessed through FESEM, water contact angle measurements, pure water flux, antifouling studies and membrane rejections. In comparison to the other developed membranes, PVDF-2 with 0.3 wt% E-CNS loading displayed optimal performance, pure water flux (PWF) of ~318.90 L m^{-2} h^{-1}, flux recovery ratio (FRR) > 90% up to three cycles, improved contact angle (80.24° to 68.44°) and reduced roughness. Furthermore, PVDF-2 achieved dye rejection of methyl orange (MO – 93.2%) and rhodamine B (RB – 94.6%), and antibiotic rejection of amoxicillin (AM – 93.8%) and tetracycline (TC – 94.1%), respectively. These findings demonstrate the integration of E-CNS derived from a bio-source, making them a promising additive to improve PVDF membrane performance.

Received 7th July 2025
Accepted 13th October 2025

DOI: 10.1039/d5na00661a

rsc.li/nanoscale-advances

1. Introduction

Water serves as a fundamental resource that sustains life and ensures the well-being of humans and other life forms.[1] With the rapid improvement in living standards and ongoing industrial and technological development, water pollution has become an increasingly critical concern. Dyes widely used in food, cosmetic and textile sectors are often toxic and non-degradable. Each year, approximately 800 000 tons of synthetic dyes are manufactured, which results in widespread water pollution.[2] Also, most of the antibiotics are water soluble and enter the aquatic environment though sewage systems following consumption and excretion by humans and animals in feces.[3] Membrane technology is an emerging and promising approach due to its efficiency and cost effectiveness for a wide range of separation and purification applications. This is supported by the advancement of sustainable methods aimed at effectively removing pollutants from contaminated water.[4] Polyvinylidene fluoride (PVDF),[5] polysulfone (PSU),[6] cellulose acetate (CA),[7] polyethersulfone (PES)[8] and polyacrylonitrile (PAN)[9] are commonly used polymers in the production of membranes. Among them, PVDF stands out due to its notable thermal stability, chemical resistance and ease of production.[10] PVDF readily dissolves in various solvents such as *N*,*N*-dimethylacetamide (DMAc), *N*,*N*-dimethylformamide (DMF), *N*-methyl-2-pyrrolidone (NMP), acetone and tetrahydrofuran (THF), which helps in the fabrication of porous membranes by several methods involving simple phase inversion protocols. These methods represent the predominant industrial approaches for large scale membrane manufacturing.[11] The inherent hydrophobicity of PVDF facilitates foulant adhesion, which undermines the efficiency of membranes over prolonged usage.[12,13] To further improve surface wettability, hydrophilicity and charge, a range of functional groups such as amine ($-NH_2$), hydroxyl (–OH), carboxyl group (–COOH) and sulphonic acid ($-SO_3H$) have been introduced into the polymer backbone.[14] Hydrophilic additives such as polyvinyl alcohol (PVA), polyethylene glycol (PEG) and polyvinylpyrrolidone (PVP) are commonly incorporated into PVDF to enhance wettability and minimize membrane fouling. However, there is still a need for the development of functional nanomaterials to improve membrane performance.[15] The modification of PVDF membranes using nanofillers such as carbon nanomaterials has gained significant attention.[16] Carbon nanoparticles (CNPs) are mainly derived from graphite and petrochemical production. These carbon-based materials produced primarily from fossil fuels have seen a significant surge in demand. This increasing demand is creating a supply shortage, leading nations to develop alternative, abundant and

[a]*Department of Chemistry, Christ University, Bengaluru-560029, Karnataka, India*
[b]*Centre for Advanced Research and Development (CARD), Christ University, Bengaluru-560029, Karnataka, India. E-mail: murthyhegde@gmail.com*
[c]*Innovation and Translational Research Hub (iTRH) & Department of Chemistry, School of Engineering, Presidency University, Bengaluru-560064, Karnataka, India*
[d]*Department of Materials Engineering, Indian Institute of Science, Bengaluru-560012, Karnataka, India*

sustainable carbon sources. Biomass, including agricultural crops and their associated waste products,[17] wood wastes and residues from forestry,[18] household and food waste,[19] municipal solid waste,[20] represents a viable and sustainable source for CNP production. Incorporation of carbon quantum dots obtained from carbonization of oil palm empty fruit bunches into PSU membrane *via* the phase inversion process, as demonstrated by Mahat *et al.*, led to improvement in pure water flux and antibacterial performance.[21] Habibi *et al.* demonstrated the incorporation of activated carbon derived from walnut shell into PES membrane showed enhanced heavy metal removal and FRR.[22] Rybarczyk *et al.* developed nitrogen functionalized carbon quantum dots using biomass to strengthen the antibiofouling properties of membranes.[23] These findings reveal that CNPs sourced from biomass significantly enhances membrane performance, suggesting a promising alternative.

The renewability and abundance of biomass make it a sustainable carbon feedstock for CNP synthesis. Latest developments have demonstrated the conversion of agricultural and lignocellulosic waste into CNPs for membrane modification. Notably, heating biomass under an inert atmosphere generates carbon nanospheres (CNS), a stable and biocompatible carbon form with low toxicity, making them ideal for materials science and water treatment applications.[24] To explore the potential of bioresources for CNS synthesis, we employed rice husk (RH), a byproduct of rice cultivation. With rice grown in more than 75 countries, the global production of rice husk has reached around 120 million tons annually.[25,26] With a rich lignocellulosic composition, rice husk comprising significant portions of cellulose (32.24%), lignin (21.44%) and hemicellulose (21.34%) offers strong potential for carbon material production.[27] Ethylenediamine functionalization to biomass derived carbon nanospheres has not been widely explored in membrane filtration. The presence of amine groups enhances the hydrophilicity by forming a hydration layer on the membrane surface by increasing the water flux and reduces fouling, thus highlighting the novelty of this work. Using the waste-to-wealth concept to convert waste materials into valuable products is a visionary step forward by creating an intersection between agriculture and nanoscience.

This study presents the development of novel E-CNS using RH through the pyrolysis method, followed by oxidation and amidation. The E-CNS were integrated into PVDF membranes to improve hydrophilicity and antifouling properties. The prepared PVDF/E-CNS membranes were employed to remove hazardous dyes and antibiotics such as rhodamine B, methyl orange, tetracycline and amoxicillin. This underscores the potential of using a bio-source based nanomaterial as a sustainable and cost-effective solution for water remediation.

2. Experimental

2.1. Materials and reagents

Rice husk was used as a raw material for the synthesis of E-CNS, and was obtained from the Western Ghats of India. Polyvinylidene fluoride (PVDF, M_w = 534 000 g mol^{-1}), polyvinylpyrrolidone (PVP, M_w = 29 000 g mol^{-1}) and bovine serum albumin (BSA, M_w = 66 430 g mol^{-1}) were obtained from Sigma Aldrich. 1-[Bis(dimethylamino)methylene]-1*H*-1,2,3-triazolo [4,5-*b*]pyridinium 3-oxid hexafluorophosphate (N-HATU), ethylenediamine (EDA), and *N*,*N*-dimethylacetamide (DMAc), obtained from Avra Synthesis Pvt. Ltd, were used as received. Hydrochloric acid (Conc. HCl), nitric acid (Conc. HNO_3) and sulphuric acid (Conc. H_2SO_4) were procured from Finar Chemicals Pvt. Ltd. The chemicals employed in this work were of analytical grade and used as received.

2.2. Synthesis and modification of rice husk derived carbon nanospheres (RH-CNS)

The RH was initially washed with water and then dried to eliminate any residual moisture. Without applying any chemical pretreatment, the dried RH was finely powdered using a mixer and sieved through a 75 μm mesh to obtain uniform particle size. The powdered RH underwent pyrolysis at 800 °C under a nitrogen atmosphere, employing a quartz tube furnace with a controlled heating rate of 10 °C per min. Comprehensive synthesis is detailed in our earlier works.[28] Following synthesis, the obtained material was washed with 0.1 N HCl and Deionised water (DIW). The sample was designated as RH-CNS and processed for further characterization and modification. RH-CNS were treated with a 3 : 1 (v/v) mixture of concentrated sulphuric acid (H_2SO_4) and nitric acid (HNO_3) under sonication at 40 °C for 3 h to introduce surface oxygen functionalities. The mixture was then filtered, washed with DIW until neutral pH was reached and dried at 80 °C for 8 h. The final product was designated as acid functionalized carbon nanospheres (O-CNS). In brief O-CNS (100 mg) were dispersed in EDA (60 cm^3). Following this, N-HATU (8 mg) was added as a coupling agent and the mixture was sonicated at 40 °C for 4 h. The resulting product was diluted with methanol (300 cm^3) and filtered, and washed several times with methanol, as described by Vuković *et al.*[29] The final product was labeled as ethylenediamine modified carbon nanospheres (E-CNS) and the schematic representation is depicted in Fig. 1.

2.3. Preparation of PVDF/E-CNS membranes

The NIPS method was used to prepare control PVDF and E-CNS integrated PVDF membranes.[30] Specifically, predetermined

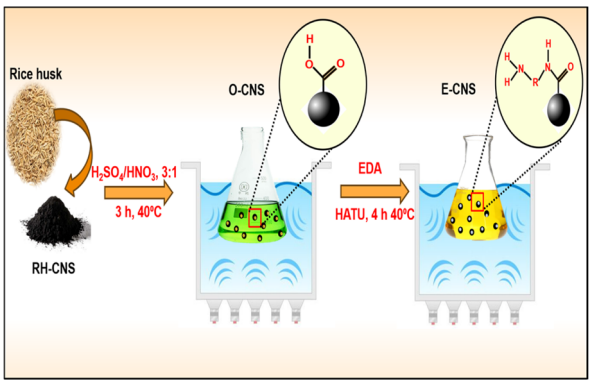

Fig. 1 Schematic representation of the methodology involved in E-CNS synthesis.

Table 1 Composition of the casting solutions

Membrane	PVDF (wt%)	PVP (wt%)	E-CNS (wt%)	DMAc (wt%)
PVDF-0	16	2	0	82
PVDF-1	16	2	0.1	81.9
PVDF-2	16	2	0.3	81.7
PVDF-3	16	2	0.5	81.5
PVDF-4	16	2	0.7	81.3

amounts of PVDF and PVP were dispersed in a mixture of DMAc and E-CNS/DMAc with varying relative weights. The solution was stirred magnetically at 60 °C for 24 h to ensure homogeneity, followed by degassing to remove entrapped air bubbles. The resulting casting solution was spread onto a clean glass plate using a film with a gap set at 120 μm. The membranes were subsequently immersed in DIW for 24 h to complete the phase inversion process and then dried before further use. To evaluate the effect of E-CNS on the performance of PVDF membranes, different E-CNS loadings (0.1, 0.3, 0.5 and 0.7 wt%) were incorporated as outlined in Table 1. The description of membrane codes and CNS variants is presented in Table S1. A schematic representation of the methodology is presented in Fig. 2.

2.4. Membrane porosity

The porosity of the pristine PVDF and PVDF/E-CNS composite membranes was measured using a gravimetric technique.[31] The porosity (ε) of the membrane was determined from the measured weights of the samples under different conditions, as described in eqn (1).

$$\varepsilon = \frac{\frac{m_1 - m_2}{\rho_w}}{\frac{m_1 - m_2}{\rho_w} + \frac{m_2}{\rho_p}} \quad (1)$$

where m_1 and m_2 are the wet and dry weights of the membranes (g) and ρ_w and ρ_p are the densities of water (0.998 cm^3) and PVDF, respectively.

2.5. Membrane performance

2.5.1. Pure water flux (PWF). The evaluation of membrane filtration efficiency involves measuring PWF. An experiment was conducted using a cross-flow filtration system using 45 mm diameter membrane discs, subjected to transmembrane pressures in the range of 25–100 psi at 25 °C. The PWF (J_w) was calculated using eqn (2).

$$J_w = \frac{V}{A \times t}\ \mathrm{L\ m^{-2}\ h^{-1}} \quad (2)$$

where A (m^2) is the effective membrane area, V (L) is the permeate volume, and t (h) is the filtration time.

2.5.2. Antifouling studies. The antifouling properties of the membranes were assessed using 1000 ppm BSA solution. Initially, membranes were exposed to DIW for 1 h and the pure water flux (J_1) was recorded every 10 min. Later, BSA solutions were filtered for 1 h and the flux (J_2) was measured. Then, the membranes were thoroughly washed and pure water flux (J_3) was recorded again for 60 min.[32] The antifouling behavior was quantified through the flux recovery ratio (FRR), total fouling (R_t), reversible fouling (R_r) and irreversible fouling (R_{ir}), as defined by the equations below:

$$\mathrm{FRR} = \frac{J_3}{J_1} \times 100\% \quad (3)$$

$$R_t(\%) = \left(1 - \frac{J_2}{J_1}\right) \times 100\% \quad (4)$$

$$R_r(\%) = \left(\frac{J_3 - J_2}{J_1}\right) \times 100\% \quad (5)$$

$$R_{ir}(\%) = \left(\frac{J_1 - J_3}{J_1}\right) \times 100\% \quad (6)$$

2.5.3. Membrane rejection performance. Model contaminants, including two dyes (methyl orange and rhodamine B) and two antibiotics (amoxicillin and tetracycline) were used as

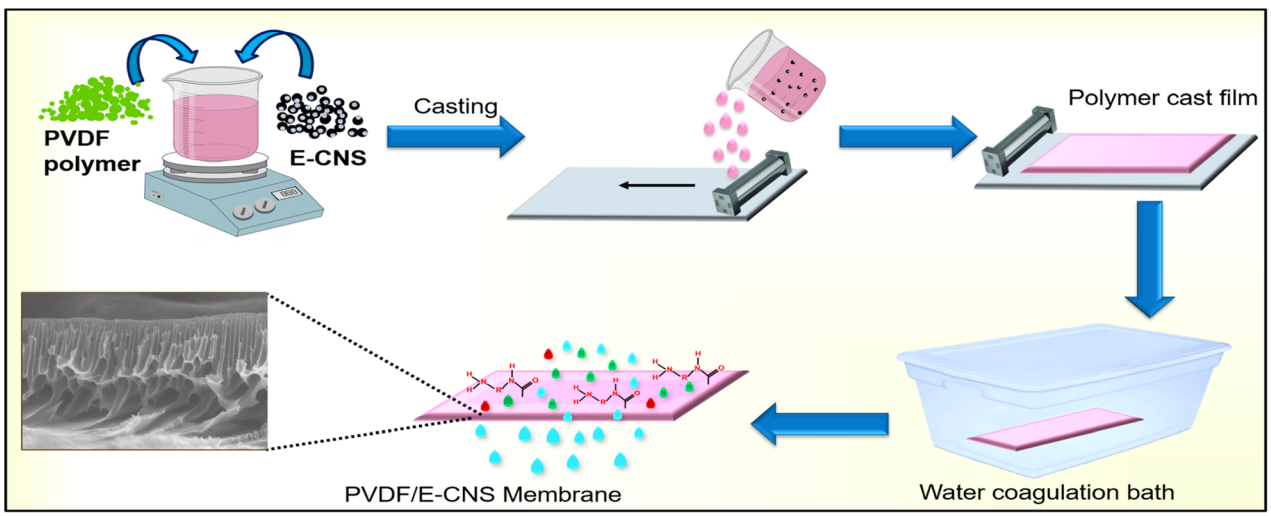

Fig. 2 Schematic illustration of PVDF/E-CNS membrane fabrication.

model contaminants. A dead-end filtration setup was employed to evaluate the rejection performance. Rejection percentage ($R\%$) was calculated according to eqn (7), where C_f and C_p represent the feed and permeate concentrations. Quantitative analysis was performed *via* UV-Vis spectrophotometry and corresponding characterization peaks (λ_{max}), as indicated in Table S2.

$$R\% = \left(1 - \left(\frac{C_p}{C_f}\right)\right) \times 100\% \quad (7)$$

3. Results and discussion

3.1. Characterization of nanoparticles

The surface morphology and elemental composition were analyzed using FESEM-EDS. The synthesized RH-CNS and E-CNS exhibited distinct spherical cluster structures as depicted in Fig. 3(a, b) and S1. The clustering of these spherical particles may be attributed to controlled reaction duration combined with a controlled cooling process from the synthesis temperature down to ambient conditions.[33] The elemental composition of RH-CNS and E-CNS was analyzed using EDS as depicted in Fig. 3(c and d). In the case of RH-CNS, carbon comprises ~85.28% and oxygen ~14.72%. Further E-CNS, confirms the presence of carbon (~62.83%), nitrogen (~18.75%) and oxygen (~18.42%). The increase in oxygen content is due to the oxidative treatment and the presence of nitrogen content signifies the successful ethylenediamine modification of RH-CNS. TEM images presented in Fig. S2 confirm the spherical morphology and nano-size of E-CNS. Together, the FESEM and TEM analysis indicates that the rice husk can be efficiently converted into carbon nanospheres with well-defined morphology, representing an emerging class of eco-friendly nanomaterials produced through a sustainable, catalyst-free pyrolysis method. The XRD patterns of RH-CNS and E-CNS, shown in Fig. 4(a), display broad diffraction peaks at approximately $2\theta = 23°$ and $2\theta = 44°$, which are typically associated

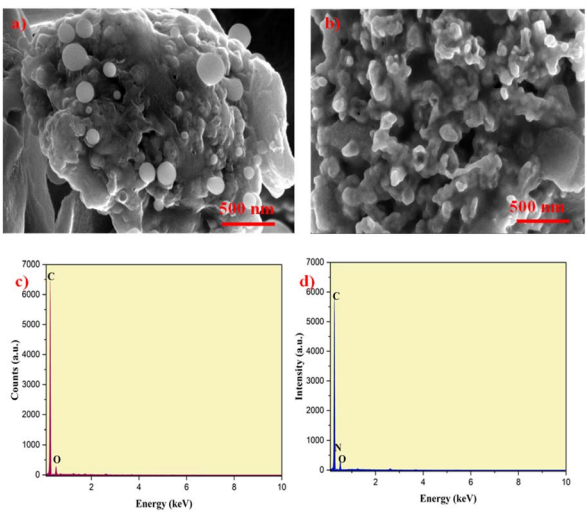

Fig. 3 FESEM images of (a) RH-CNS and (b) E-CNS, EDS spectrum of (c) RH-CNS and (d) E-CNS.

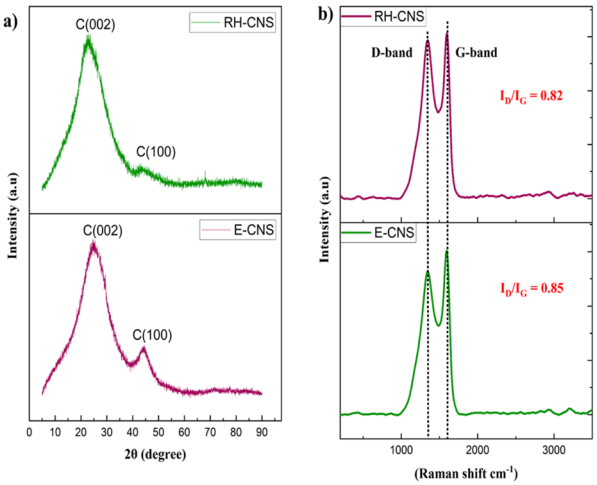

Fig. 4 (a) XRD patterns of RH-CNS and E-CNS, (b) Raman spectrum of RH-CNS and E-CNS.

with the (002) and (100) planes of the amorphous carbon structures which are commonly found in turbostratic carbon.[34] A broad (002) peak reflects poor graphitization and an irregular arrangement of carbon layers. The (100) peak indicates the development of a honeycomb composed of sp^2 hybridized carbons, which aligns well with the earlier reports.[35–38] EDA modification may induce local ordering of carbon domains, thereby strengthening the π–π stacking between the carbon layers. This improvement in layer alignment increases the crystallinity of the material, causing the corresponding peak to become more pronounced and well defined. Raman spectroscopy is employed to study molecular vibrations and rotational energies, enabling material identification. It is also extensively used to investigate the structural characteristics of carbon-based materials. The Raman spectra of RH-CNS and E-CNS reveal two prominent bands as depicted in Fig. 4(b). The D-band, observed at approximately 1337 cm^{-1} for RH-CNS and 1363 cm^{-1} for E-CNS, corresponds to the A_{1g} vibrational mode and indicates structural disorder due to sp^3 hybridized carbon. In contrast, the G-band located at approximately 1598 cm^{-1} and 1597 cm^{-1}, is ascribed to the E_{2g} mode of vibration, which is indicative of sp^2 hybridized C–C bonding in the graphitic framework. The relative intensity ratio (I_D/I_G) is critical in evaluating graphitic features. RH-CNS and E-CNS exhibited an I_D/I_G ratio of approximately 0.83 and 0.85, respectively. The slight increase in I_D/I_G ratio suggests a greater degree of covalent functionalization.

The FTIR spectra of the rice husk (RH-Raw), RH-CNS, O-CNS and E-CNS are illustrated in Fig. 5(a). In RH-Raw, a broad band observed at approximately 3300 cm^{-1} is characteristic of O–H stretching vibrations which are associated with hydroxyl groups in cellulosic components. The absorption at ~2912 cm^{-1} is indicative of C–H stretching and the peak at ~1730 cm^{-1} reveals the presence of carbonyl groups, signifying a notable amount of oxygen based functional groups in the sample.[24] The distinct absorption bands at ~1221 and 1022 cm^{-1} are attributed to C–O–C glycosidic linkages found in hemicellulose and

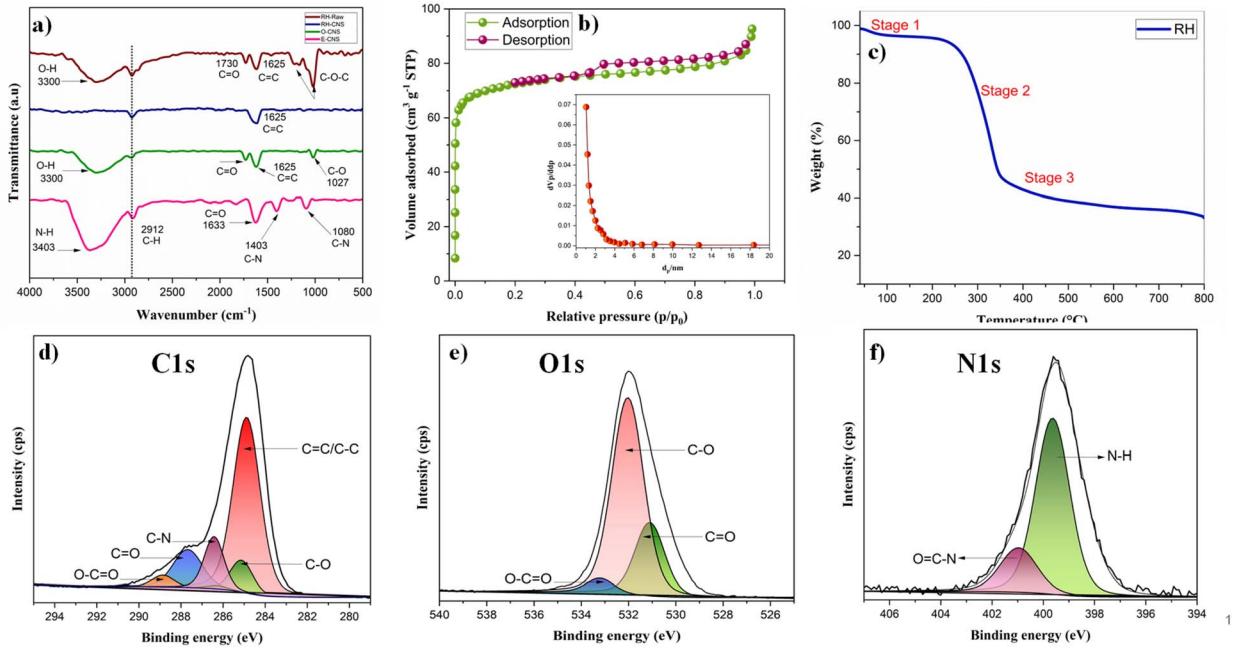

Fig. 5 (a) FTIR spectrum of RH-Raw, RH-CNS, O-CNS and E-CNS, (b) N_2 adsorption–desorption isotherm and pore size distribution of E-CNS, (c) TGA curve of RH, XPS spectrum of E-CNS: (d) C1s, (e) O1s, (f) N1s.

cellulose. However, RH-CNS exhibited a reduction in oxygen content which is due to higher synthesis temperature that promoted the loss of oxygenated functional groups. For O-CNS, oxidative treatment using a mixture of concentrated H_2SO_4 and HNO_3 resulted in the formation of carboxyl groups on the surface of RH-CNS. This was confirmed by the appearance of distinct peaks at approximately 3300 cm^{-1} and 1730 cm^{-1}, which corresponds to the stretching vibrations of hydroxyl (–OH) and (C═O) groups in carboxylic acids. In the case of E-CNS, the bands occurring at ~1633 cm^{-1} and ~1403 cm^{-1} are indicative of the symmetric stretching vibrations of the carbonyl (C═O) and the C–N bonds in amide groups, while the peak at ~1080 cm^{-1} corresponds to the stretching vibration of the C–N bond in amines.[29] The peak at ~3403 cm^{-1} was due to the NH_2 stretching of the amine group. The FTIR analysis verifies that amides are covalently attached to O-CNS. The specific surface area of E-CNS was analyzed using the Brunauer–Emmett–Teller (BET) method and depicted in Fig. 5(b). The nitrogen adsorption–desorption isotherm of E-CNS displayed a type IV hysteresis loop, with a BET surface area of 279.56 m^2 g^{-1} and an average pore diameter of 2.02 nm. These findings confirm the mesoporous nature and porous structure of E-CNS, supporting the suitability of the material for membrane fabrication and contributing to enhanced rejection efficiency. The TGA curve illustrates the thermal decomposition behavior of the precursor as illustrated in Fig. 5(c). Biomass is primarily composed of hemicellulose, cellulose, lignin and minor contributions from vitamins and extractives. The sample was subjected to thermal treatment under a nitrogen atmosphere, with the temperature ramping from 30 to 800 °C at a rate of 10 °C min^{-1}. The initial weight loss of ~8% observed between 100 and 250 °C is primarily due to the evaporation of moisture.[39] The major weight loss between 250 and 400 °C reflects the breakdown of hemicellulose and cellulose present in rice husk and the following mass reduction is due to decomposition of lignin. Approximately 50% of the material mass loss was lost during this stage, driven by elimination of volatiles from the precursor. Besides, weight loss is minimal, suggesting the formation of thermally stable structures with enhanced carbon content. To ensure complete carbonization, the process was continued up to 800 °C, yielding high purity carbon. Further confirmation of ethylenediamine functionalization on O-CNS was also provided by XPS analysis (Fig. 5(d–f)), indicated by the presence of the N1s spectrum. The C1s XPS spectrum showed five distinct peaks at 284.9 eV, 285.1 eV, 286.4 eV, 287.72 eV and 289.3 eV, corresponding to C═C/C–C, C–O, C–N, C═O and O–C═O bonds on E-CNS.[40] In addition, O1s spectra exhibited three distinct peaks at 531.1 eV, 532.01 eV and 533.7 eV, which can be attributed to C═O, C–O and O–C═O functional groups.[41] The N1s spectrum displayed two characteristic peaks at 399.7 eV and 401.10 eV, associated with N–H and N–C═O groups, respectively.[42,43] These findings verified the effective EDA modification through amide bond formation, aligning well with the FTIR results.

3.2. Membrane characterization

The morphological features including both surface and cross-sections of the prepared membranes are shown in the FESEM images presented in Fig. 6(a–j). The membrane exhibits an asymmetric structure constituting a dense upper layer with fine pores, which serves as a selective barrier. The upper surface remains smooth and shows no obvious defects. Based on eqn (1) the porosity of the E-CNS integrated membranes increased significantly. This is attributed to the addition of E-CNS, which

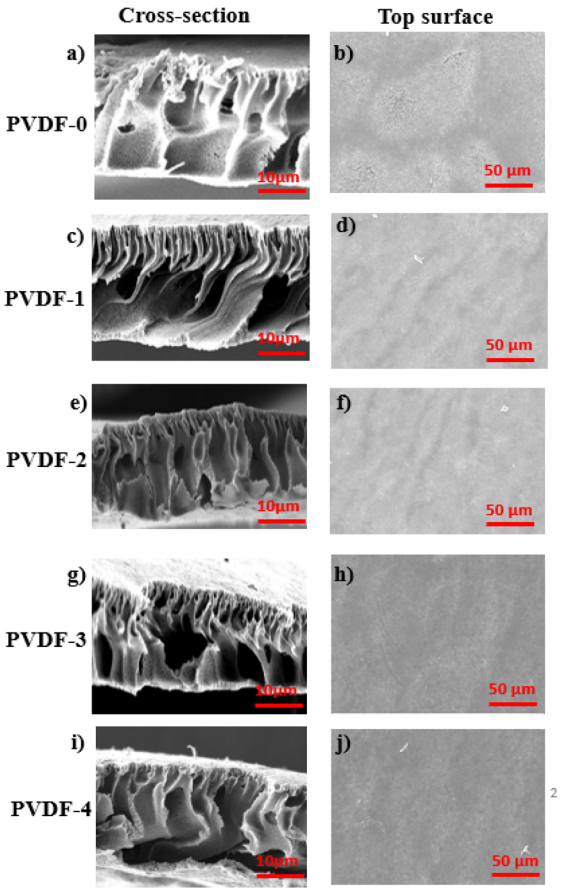

Fig. 6 (a, c, e, g and i) Cross sectional view, (b, d, f, h and j) top surface of pristine PVDF and PVDF/E-CNS composite membranes.

enhances the solvent–nonsolvent exchange rate and facilitates the development of larger pores, leading to enhanced porosity of the membranes. Nonetheless, the increased E-CNS loading may result in particle agglomeration, which hinders solvent–nonsolvent exchange and negatively affects pore development.[44] The E-CNS distribution on the membranes was evaluated using EDS mapping and depicted in Fig. S3. While the addition of E-CNS causes minimal morphological changes, it is anticipated that E-CNS significantly enhance the hydrophilicity and boost the water permeability of the membrane. Table S3 reveals that porosity increases as E-CNS content is raised to 0.3 wt%. At 0.5 wt% a reduction in porosity is noted due to the agglomeration of the nanofillers, which disrupts the solvent exchange rate and limits pore expansion. The thermal stability of the composite membranes was examined using TGA as depicted in Fig. 7(b). As shown in the TGA curves, all the membranes displayed a similar weight loss behavior. The mass of the PVDF membranes stayed nearly unchanged (~100%) from 0 to 350 °C, indicating its high decomposition temperature.[31] The rightward shift in TGA curves observed for PVDF-2 (0.3 wt% E-CNS) relative to PVDF-0 suggests a considerable enhancement in thermal stability with E-CNS addition. PVDF-0 began decomposing at 340 °C, with weight loss (3–5%) at ~350 °C, followed by a rapid reduction (~55%) between 350 and 500 °C. Beyond 500 °C, both pristine PVDF and PVDF/E-CNS composite membranes showed negligible weight changes. Final weight losses were 58.0% for PVDF-0 and 60.02%, 61.25%, 62.05% and 62.35% for membranes with 0.1–0.7 wt% E-CNS loading. Carbonization of degradation residues continued until 800 °C. The FTIR measurements of PVDF and PVDF/E-CNS membranes were recorded in the spectral range of 4000 to 400 cm^{-1} and presented in Fig. 7(a). PVDF-0 exhibited characteristic bands at 1170 and 2917 cm^{-1}, associated with the C–F stretching and CH_2 group deformation vibrations. The band at 1404 cm^{-1} was attributed to CH_2 group deformation vibrations. Additionally, the bands at 870 and 840 cm^{-1} were assigned to the rocking mode of vinylidene groups within the polymer matrix. A comparable pattern is observed in the FTIR spectra of E-CNS integrated PVDF membranes and pristine PVDF membranes, which is consistent with the reported findings.[47] Additionally, the PVDF/E-CNS composite membranes displayed notable peaks at 1735 cm^{-1} and 3340 cm^{-1} corresponding to the carbonyl and N–H stretching vibrations of amine groups.[15,48] This suggests that hydrophilic groups from E-CNS contribute to the development of hydrophilic layers on the membrane surface.

The surface wettability of the prepared membranes was evaluated using WCA using the sessile drop method with a goniometer. This test was conducted on membrane samples to detect changes in wettability associated with different concentrations of E-CNS. Membrane hydrophilicity plays a crucial role in determining water flux and resistance to fouling as it indicates the tendency of the surface to attract or repel water.[49] Fig. 7(c) shows that PVDF-0 exhibited the highest hydrophobicity, with a WCA of 80.24°, which aligns with previously reported measurements.[50] Conversely, the WCA decreased to 68.44°, suggesting that the incorporation of E-CNS enhances the hydrophilicity of the membrane. However, a slight increase in WCA was observed when the E-CNS content rose from 0.5 to 0.7 wt%, likely due to agglomeration and pore blockage caused by excessive addition of E-CNS. The surface

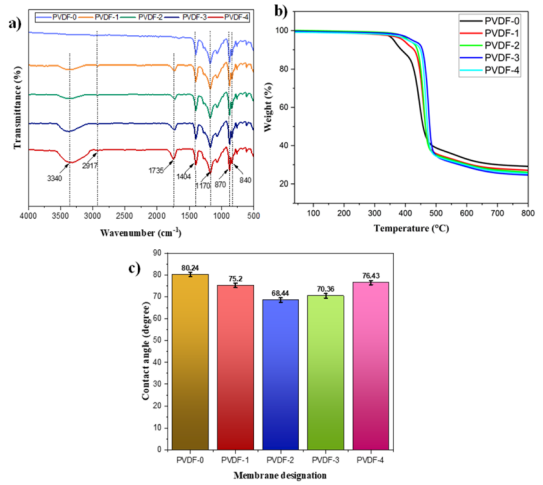

Fig. 7 (a) FTIR spectrum, (b) TGA curves, and (c) WCA measurements of pristine PVDF and PVDF/E-CNS membranes.

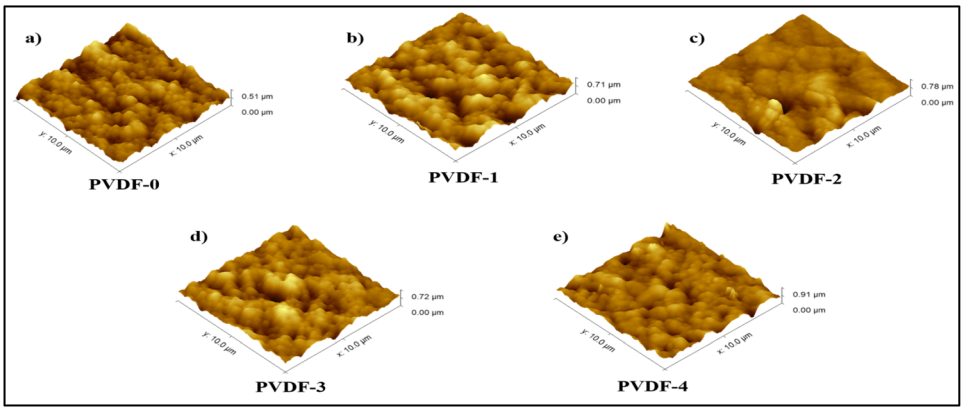

Fig. 8 AFM images of (a) pristine PVDF-0, (b) PVDF-1 (0.1 wt% E-CNS), (c) PVDF-2 (0.3 wt% E-CNS), (d) PVDF-3 (0.5 wt% E-CNS) and (e) PVDF-4 (0.7 wt% E-CNS) membranes.

roughness of a membrane is a key factor in evaluating antifouling performance.

A smoother surface offers fewer sites for pollutant adsorption, thereby enhancing resistance to fouling.[45] AFM was utilized to analyze the influence of E-CNS on the surface roughness of the PVDF/E-CNS composite membranes as depicted in Fig. 8(a–e). The pristine PVDF membrane exhibited a comparatively rougher surface than the E-CNS incorporating membranes. This observation indicates that the addition of hydrophilic additives contributed to reduced roughness. Notably, PVDF-2 (0.3 wt% E-CNS) displayed the lowest average roughness (S_a) of 418 nm and RMS roughness (S_q) of 96 nm, respectively. This was attributed to the effective dispersion of the E-CNS additives within the polymer matrix, resulting in a smoother and less wrinkled membrane surface.

At higher loading of E-CNS (PVDF-4), the surface roughness increased significantly, with S_a of 518 nm and S_q of 89 nm, surpassing that of the control membrane as shown in Table 2. This increase can be attributed to interactions among E-CNS particles themselves, where extensive cross-linking *via* hydrogen bonding occurs at additive levels above 0.3 wt%, causing particle agglomeration. These agglomerated particles act as physical barriers that hinder the counter diffusion between the solvent and non-solvent phases.[46]

3.3. Membrane performance

3.3.1. Pure water flux. Membrane performance was initially evaluated through pure water flux and calculated using eqn (2) as depicted in Fig. 9(a). The studies were carried out using DIW at transmembrane pressures in the range of 25–100 psi. The results indicate a linear increase in PWF, which is comparable to that of PVDF-0. All E-CNS composite membranes exhibited enhanced PWF, with PVDF-2 (with 0.3 wt% E-CNS) achieving the highest flux value of 318.90 L m^{-2} h^{-1}. The PWF increased with 0.3 wt% E-CNS but further increase in E-CNS content led to the reduction of flux. The same trend was observed by Z. Zheng *et al.*[51] At higher concentrations, E-CNS tends to agglomerate, thereby reducing the membrane porosity and hydrophilicity, and consequently lowering the PWF.[52]

3.3.2. Antifouling performance of membranes. Membrane performance is often limited by fouling, which includes pore blockage, cake layer, organic matter adsorption, biofouling and inorganic scaling, resulting in temporary or irreversible flux decline.[53] A three-cycle ultrafiltration test was conducted to assess the antifouling properties of the PVDF/E-CNS membranes. Bovine albumin serum (BSA) solution served as

Table 2 Surface roughness values of pristine PVDF and PVDF/E-CNS composite membranes

	Surface roughness	
Membrane	S_a (nm)	S_q (nm)
PVDF-0	472	96
PVDF-1	449	70
PVDF-2	418	60
PVDF-3	425	87
PVDF-4	518	89

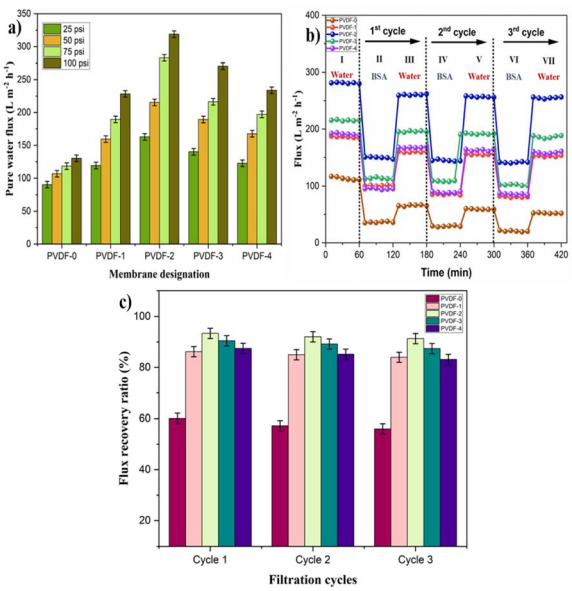

Fig. 9 (a) PWF, (b) time dependent BSA flux, (c) flux recovery ratios in three cycles of pristine PVDF and PVDF/E-CNS membranes.

the model of foulant in this evaluation. The resulting time-dependent flux profiles are illustrated in Fig. 9(b). The experiment involves alternating steps of PWF (I, III, V, VII) and BSA flux (II, IV, VI). A notable decline in flux was observed when BSA solution was used as feed. This is primarily due to deposition of BSA on the surface of the membrane.[54] Eqn (3) was used to calculate the FRR, which measures the ability of the membrane to recover the flux after BSA fouling.

The improved antifouling performance of the membranes is reflected by the high FRR value as shown in Fig. 9(c). In the first cycle, the membranes exhibited improved FRRs of 60.1% (PVDF-0), 86.17% (PVDF-1 with 0.1 wt% E-CNS), 93.36% (PVDF-2 with 0.3 wt% E-CNS), 90.46% (PVDF-3 with 0.5 wt% E-CNS), and 87.46% (PVDF-4 with 0.7 wt% E-CNS). The improved FRR observed in the PVDF-2 membrane demonstrates better antifouling properties, which is attributed to its hydrophilicity and reduced surface roughness. The functionalization process predominantly introduces amide groups which improves the hydrophilicity of the membranes. Addition of E-CNS substantially improves antifouling properties by facilitating the development of a hydration layer which inhibits the attachment of the foulant and improves the membrane performance. The polar nature of amide groups enables hydrogen bonding with water, thereby increasing water affinity and reducing the BSA adhesion on the membrane surface. The original flux values could not be fully restored, due to protein entrapment within the membrane pores. However, higher PWFs were observed across all the E-CNS incorporating membranes when compared to the unmodified PVDF membrane. PVDF-2 (with 0.3 wt% E-CNS) continued to show improved antifouling performance with FRRs of 91.91% and 89.9% after the second and third cycles. The antifouling characteristics of the PVDF/E-CNS composite membranes were evaluated using eqn (4)–(6), which yielded FRR, R_t, R_r and R_{ir} shown in Fig. S4. R_r corresponds to fouling that can be eliminated by cleaning, while R_{ir} indicates fouling that remains post cleaning and negatively impacts the membrane performance. Among all the tested membranes, PVDF-2 demonstrated improved performance, maintaining FRR values above 90% and R_{ir} below 8.74% across three cycles, identifying PVDF-2 with 0.3 wt% E-CNS as the most effective loading. The PVDF-2 membrane demonstrated over 33% higher BSA rejection rate compared to PVDF-0 (Table 3).

3.3.3. Membrane rejection performance. The membrane rejection performance was assessed using dyes (rhodamine B and methyl orange) and antibiotics (tetracycline and amoxicillin). These pollutants are often discharged into aquatic environments and are harmful when present in large quantities.[64,65] Dye rejection performance was evaluated for the control and PVDF/E-CNS composite membranes with 20 mg L^{-1} dye concentration, as illustrated in Fig. 10(a and b). The PVDF-2 (with 0.3 wt% E-CNS) membrane was able to reject nearly 93.21% methyl red and 94.6% rhodamine B. The selectivity of the membranes in removing the cationic dyes can be explained by the high zeta potential value (*ca.* −36.06) of PVDF-2 as shown in Fig. S5. RB was efficiently removed by all the tested membranes, with rejection rates above 85% (Fig. 10(a)). Notably, PVDF-2 (with 0.3 wt% E-CNS) and PVDF-3 (with 0.5 wt% E-CNS) exhibited superior performance, achieving 94.6% and 92.9% rejection. This is attributed to strong electrostatic interaction and strong adsorption on the surface of the membrane, thus accounting for their enhanced removal efficiency. The anionic dye (MO) being negatively charged faced electrostatic repulsion due to the presence of multiple negatively charged carboxylate groups in the MO dye and steric hindrance and thus could not enter the permeate (Fig. 10(b)). The rejection efficiency of RB and MO was assessed using a UV-Vis spectrophotometer and is depicted in Fig. S6. A combined mechanism of electrostatic attraction/repulsion and molecular sieving underlies the enhanced dye rejection performance of PVDF/E-CNS composite membranes.

With the ongoing decline in public health driven by multiple factors, including the recent pandemic, the reliance on antibiotics remains substantial and continues to rise. Amoxicillin (AM) and tetracycline (TC) were used as model pollutants with 20 mg L^{-1} concentrations as illustrated in Fig. 10(c and d). The PVDF/E-CNS membranes removed >85% of both antibiotics. This observation could be explained by the electrostatic interaction between negatively charged membranes and tetracycline moieties, whereas amoxicillin suffers from electrostatic repulsion from the PVDF/E-CNS membranes. The pore size of the membrane also contributed to the enhanced removal rates. The rejection rates of TC and AM were determined using a UV-Visible spectrophotometer (Fig. S7).

Table 3 Performance comparison of the membranes modified with different CNPs

Carbon-based nanomaterials (wt%)	Fabrication method	FRR (%)	PWF (L m^{-2} $h^{-1)}$	Reference
Mesoporous carbon nanoparticles (0.2 wt%)	NIPS	60.9	257.8	55
MWCNT-COOH (0.1 wt%)	NIPS	93	138	56
PCA-CNT (0.1 wt%)	NIPS	95	32	57
HAp/AC (4 wt%)	NIPS	93.4	660	58
GO@MOF (0.12 wt%)	NIPS	88.13	183.51	59
GO-$WO_{2.89}$	NIPS	92.66	636.01	60
GO-nanoribbons (0.5 wt%)	NIPS	86	532.28	61
Reed root derived activated carbon (0.1 wt%)	NIPS	91.14	255.77	62
rGO-PDA (0.1 wt%)	NIPS	80.4	326.5	63
Rice husk derived ethylenediamine modified carbon nanospheres (0.3 wt%)	**NIPS**	**93.43%**	**318.90**	**This work**

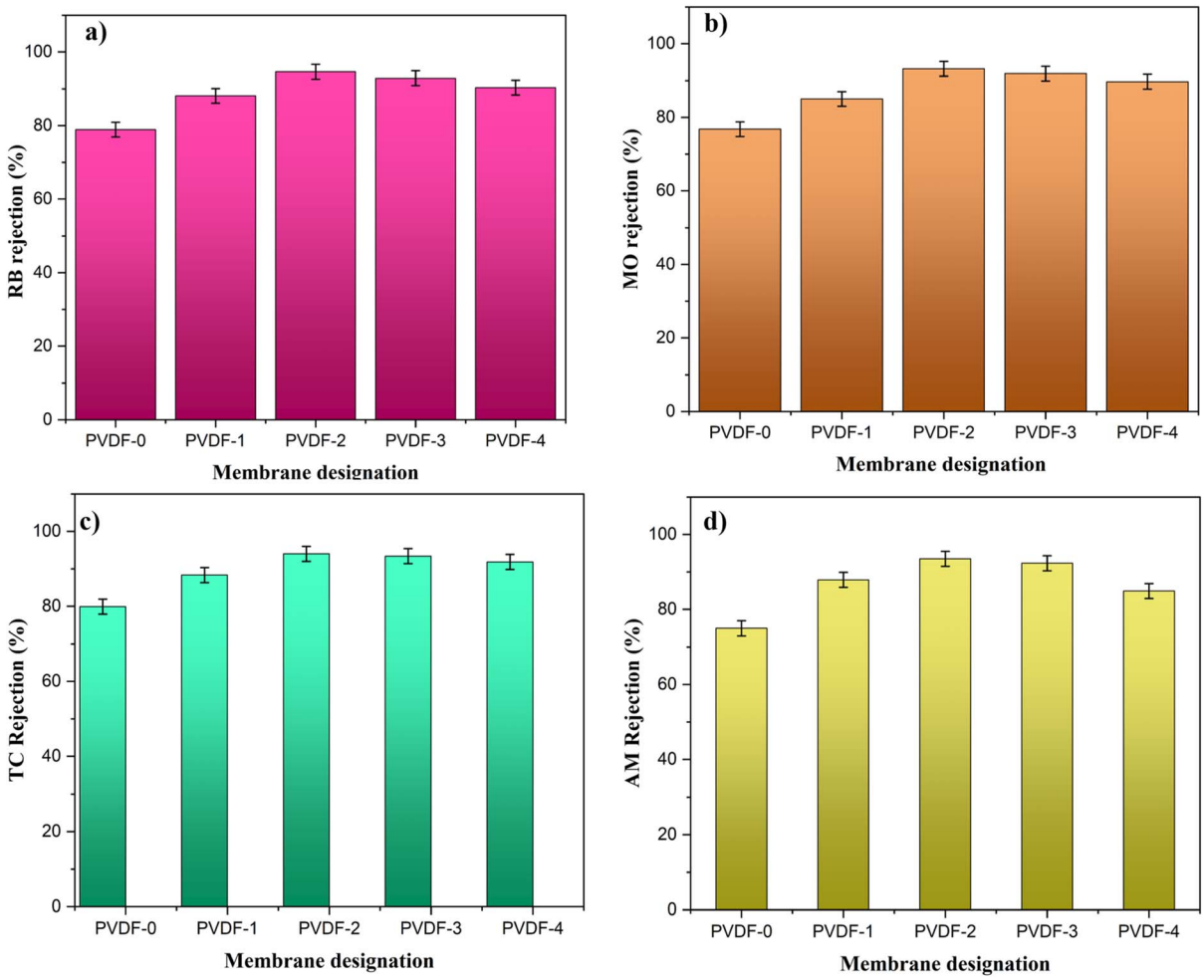

Fig. 10 Rejection rates of (a) RB, (b) MO, (c) TC and (d) AM.

4. Conclusions

In summary, ethylenediamine modified carbon nanospheres (E-CNS) were synthesized using rice husk. The developed PVDF/E-CNS composite membranes significantly improved their porosity, water affinity and reduced surface roughness compared to the pristine PVDF membrane. These enhancements promoted increased PWF, antifouling efficiency, and dye and antibiotic rejections. Among the various loadings tested, the membrane composed of 0.3 wt% E-CNS (PVDF-2) showed an increased PWF of 318.90 L m^{-2} h^{-1}, boosted rejection rates for both dyes (93.2% – MO and 94.6% – RB) and antibiotics (93.91% – AM and 94.5% – TC). The antifouling studies demonstrated FRR > 90% and R_{ir} < 8.74% over three filtration cycles, reflecting its robustness and reliability for long-term application. The novelty of this work lies in employing EDA functionalized CNS derived from agricultural waste as an effective additive for membrane filtration. The enhanced membrane performance highlights its potential for applications in treating contaminants prior to water release.

Author contributions

B. G. Maya Patel: conceptualization, methodology, data curation, investigation, validation, writing-original draft, writing-review and editing. Sk Safikul Islam: investigation, formal analysis. Samir Mandal: data curation, resources. Suryasarathi Bose: data curation, resources, writing-review & editing. Gurumurthy Hegde: conceptualization, methodology, supervision, validation, funding acquisition, writing-review & editing.

Conflicts of interest

There are no conflicts to declare.

Data availability

The data supporting this article have been included as part of the supplementary information (SI). Supplementary information is available. See DOI: **https://doi.org/10.1039/d5na00661a**.

Acknowledgements

We thank the Central Instrumentation Facilities, Christ University for providing the instrument facilities and CENSE and IPC for characterization support. One of the author GH thank the RKVY Raftaar, UAS Dharwad for providing grant under Avishakar Scheme.

References

1 S. Dutta, S. K. Srivastava and A. K. Gupta, *Mater. Adv.*, 2021, **2**, 2431–2443.
2 H. B. Slama, A. Chenari Bouket, Z. Pourhassan, F. N. Alenezi, A. Silini, H. Cherif-Silini, T. Oszako, L. Luptakova, P. Golińska and L. Belbahri, *Appl. Sci.*, 2021, **11**, 6255.
3 B. Halling-Sørensen, *Arch. Environ. Contam. Toxicol.*, 2001, **40**, 451–460.
4 M. S. Kanth, S. L. Sandhya Rani and V. K. Raja, *Hybrid Adv.*, 2025, **8**, 100380.
5 Z. Li, W. Wang, C. Ndahiro, X. Zhou, S. Shen and G. Zhang, *J. Water Process Eng.*, 2025, **74**, 107896.
6 H. U. Modekwe, I. M. Ramatsa, M. A. Mamo, O. O. Sadare, M. O. Daramola and K. Moothi, *Waste Manag. Bull.*, 2025, **3**, 39–47.
7 F. Li, Y. An, J. Xue, H. Fu, H. Wang, P. Cao, M. Zhang, P. Fei, M. Liu and F. Zhao, *Small*, 2025, **21**, e2409728.
8 M. J. Raseala, M. M. Motsa, R. A. Sigwadi and R. M. Moutloali, *J. Ind. Eng. Chem.*, 2025, **145**, 596–609.
9 X. Li, J. Liu, Y. Zhang, M. Tao, N. Ma, J. Cao and W. Zhang, *J. Environ. Chem. Eng.*, 2025, **13**, 116579.
10 R. Gayatri, A. N. S. Fizal, E. Yuliwati, M. S. Hossain, J. Jaafar, M. Zulkifli, W. Taweepreda and A. N. Ahmad Yahaya, *Nanomaterials*, 2023, **13**, 1023.
11 V. Dhand, S. K. Hong, L. Li, J.-M. Kim, S. H. Kim, K. Y. Rhee and H. W. Lee, *Composites, Part B*, 2019, **160**, 632–643.
12 Z. Wang, G. Feng, Z. Yan, S. Li, M. Xu, C. Wang and Y. Li, *React. Funct. Polym.*, 2023, **189**, 105610.
13 X. Kong, Q.-Z. Wang, Y.-F. Wang, H.-M. Huo, F.-Q. Kou, S.-B. Zhang, J. Zhao, D. Zhang, L. Hao, Y.-J. Chang and D.-E. Zhang, *J. Membr. Sci.*, 2025, **715**, 123474.
14 N. S. Naik, M. Padaki, A. M. Isloor, K. K. Nagaraja and K. A. Vishnumurthy, *Chem. Eng. J.*, 2021, **418**, 129372.
15 B. G. M. Patel, S. S. Islam, S. Mandal, S. Bose and G. Hegde, *J. Environ. Chem. Eng.*, 2025, **13**, 115879.
16 J. Kujawa, S. Boncel, S. Al-Gharabli, S. Koter, W. Kujawski, K. Kaneko, K. Li, E. Korczeniewski and A. P. Terzyk, *Desalination*, 2024, **574**, 117277.
17 D. Pathania, A. Araballi, F. Fernandes, J. M. Shivanna, G. Sriram, M. Kurkuri, G. Hegde and T. M. Aminabhavi, *Environ. Res.*, 2023, **224**, 115521.
18 G. Hegde, S. A. Abdul Manaf, A. Kumar, G. A. M. Ali, K. F. Chong, Z. Ngaini and K. V. Sharma, *ACS Sustainable Chem. Eng.*, 2015, **3**, 2247–2253.
19 S. Kane and C. Ryan, *Compos., Part C: Open Access*, 2022, **8**, 100274.
20 M. S. Soffian, F. Z. Abdul Halim, F. Aziz, M. A. Rahman, M. A. Mohamed Amin and D. N. Awang Chee, *Environ. Adv.*, 2022, **9**, 100259.
21 N. A. Mahat, S. A. Shamsudin, N. Jullok and A. H. Ma'Radzi, *Desalination*, 2020, **493**, 114618.
22 R. Habibi, B. Barzegar, H. Aghdasinia and A. Khataee, *J. Environ. Chem. Eng.*, 2024, **12**, 113172.
23 M. K. Rybarczyk, E. Gontarek-Castro, K. Ollik and M. Lieder, *Processes*, 2020, **9**, 61.
24 A. Shetty, D. Sunil, T. Rujiralai, S. P. Maradur, A. N. Alodhayb and G. Hegde, *Nanoscale Adv.*, 2024, **6**, 2516–2526.
25 J. Acharya, U. Kumar and P. M. Rafi, *Int. J. Curr. Eng. Technol.*, 2018, **8**, 526–530.
26 M. Indumathi, G. Nakkeeran, D. Roy, S. K. Gupta and G. U. Alaneme, *Discover Appl. Sci.*, 2024, **6**, 597.
27 Z. Shamsollahi and A. Partovinia, *J. Environ. Manage.*, 2019, **246**, 314–323.
28 S. Yallappa, M. Shivakumar, K. L. Nagashree, M. S. Dharmaprakash, A. Vinu and G. Hegde, *J. Electrochem. Soc.*, 2018, **165**, H614–H619.
29 G. D. Vuković, A. D. Marinković, M. Čolić, M. Đ. Ristić, R. Aleksić, A. A. Perić-Grujić and P. S. Uskoković, *Chem. Eng. J.*, 2010, **157**, 238–248.
30 J. Chae, T. Lim, H. Cheng and W. Jung, *Nanomaterials*, 2021, **11**, 2269.
31 H. Yu, L. Gu, S. Wu, G. Dong, X. Qiao, K. Zhang, X. Lu, H. Wen and D. Zhang, *Sep. Purif. Technol.*, 2020, **247**, 116889.
32 X. Ma, C. Wang, H. Guo, Z. Wang, N. Sun, P. Huo, J. Gu and Y. Liu, *J. Mater. Sci.*, 2022, **57**, 6474–6486.
33 A. Shetty and G. Hegde, *React. Kinet., Mech. Catal.*, 2024, **137**, 2989–3004.
34 R. Bahadur, G. Singh, Z. Li, B. Singh, R. Srivastava, Y. Sakamoto, S. Chang, R. Murugavel and A. Vinu, *Carbon*, 2024, **216**, 118568.
35 O. Abdalla, M. A. Wahab and A. Abdala, *J. Environ. Chem. Eng.*, 2020, **8**, 104269.
36 J. Shu, S. Cheng, H. Xia, L. Zhang, J. Peng, C. Li and S. Zhang, *RSC Adv.*, 2017, **7**, 14395–14405.
37 K. Vignesh, M. Ganeshbabu, N. P. N. Puneeth, T. Mathivanan, B. Ramkumar, Y. S. Lee and R. K. Selvan, *J. Energy Storage*, 2023, **72**, 108216.
38 A. Maleki, V. Irani and A. Tavasoli, *J. Nat. Gas Sci. Eng.*, 2019, **71**, 103004.
39 A. Sharma, J. M. Shivanna, A. N. Alodhayb and G. Hegde, *Nanoscale Adv.*, 2024, **6**, 3199–3210.
40 K. Chang, Q. Zhu, L. Qi, M. Guo, W. Gao and Q. Gao, *Materials*, 2022, **15**, 466.
41 K. Jiang, X. Feng, X. Gao, Y. Wang, C. Cai, Z. Li and H. Lin, *Nanomaterials*, 2019, **9**, 529.
42 X. Chen, J. Bai, Y. Ma, G. Yuan, J. Mei, L. Zhang and L. Ren, *Microchem. J.*, 2019, **149**, 103981.
43 C. Wang, H. Shi, M. Yang, Y. Yan, E. Liu, Z. Ji and J. Fan, *Mater. Res. Bull.*, 2020, **124**, 110730.
44 P. Kallem, M. Ouda, G. Bharath, S. W. Hasan and F. Banat, *Chemosphere*, 2022, **286**, 131799.
45 A. Idris, N. Mat Zain and M. Y. Noordin, *Desalination*, 2007, **207**, 324–339.
46 A. Asadi, F. Gholami and A. A. Zinatizadeh, *Environ. Sci. Pollut. Res. Int.*, 2022, **29**, 37144–37158.

47 R. Gayatri, A. N. S. Fizal, E. Yuliwati, M. Z. Zailani, J. Jaafar, M. S. Hossain, M. Zulkifli, W. Taweepreda and A. N. Ahmad Yahaya, *Case Stud. Chem. Environ. Eng.*, 2024, **9**, 100620.
48 A. Q. Al-Gamal and T. A. Saleh, *Mater. Today Sustain.*, 2022, **20**, 100250.
49 R. S. Zambare, K. B. Dhopte, A. V. Patwardhan and P. R. Nemade, *Desalination*, 2017, **403**, 24–35.
50 Z. Guo, X. Xu, Y. Xiang, S. Lu and S. P. Jiang, *J. Mater. Chem. A*, 2015, **3**, 148–155.
51 Z. Zheng, J. Chen, J. Wu, M. Feng, L. Xu, N. Yan and H. Xie, *Nanomaterials*, 2021, **11**, 2303.
52 O. Abdalla, A. Rehman, A. Nabeeh, M. A. Wahab, A. Abdel-Wahab and A. Abdala, *Membranes*, 2023, **13**, 678.
53 A. Karkooti, A. Z. Yazdi, P. Chen, M. McGregor, N. Nazemifard and M. Sadrzadeh, *J. Membr. Sci.*, 2018, **560**, 97–107.
54 X. Liu, H. Yuan, C. Wang, S. Zhang, L. Zhang, X. Liu, F. Liu, X. Zhu, S. Rohani, C. Ching and J. Lu, *Sep. Purif. Technol.*, 2020, **233**, 116038.
55 Y. Orooji, M. Faghih, A. Razmjou, J. Hou, P. Moazzam, N. Emami, M. Aghababaie, F. Nourisfa, V. Chen and W. Jin, *Carbon*, 2017, **111**, 689–704.
56 S. Gholami, J. L. Llacuna, V. Vatanpour, A. Dehqan, S. Paziresh and J. L. Cortina, *Chemosphere*, 2022, **294**, 133699.
57 P. Daraei, S. S. Madaeni, N. Ghaemi, M. A. Khadivi, B. Astinchap and R. Moradian, *J. Membr. Sci.*, 2013, **444**, 184–191.
58 P. Kallem, M. Ouda, G. Bharath, S. W. Hasan and F. Banat, *Chemosphere*, 2022, **286**, 131799.
59 S. Yang, Q. Zou, T. Wang and L. Zhang, *J. Membr. Sci.*, 2019, **569**, 48–59.
60 R. M. Al-Maliki, Q. F. Alsalhy, S. Al-Jubouri, A. A. AbdulRazak, M. A. Shehab, Z. Németh, K. Hernadi and H. S. Majdi, *Membranes*, 2023, **13**, 269.
61 M. A. Tofighy, T. Mohammadi and M. H. Sadeghi, *J. Appl. Polym. Sci.*, 2020, 49718.
62 Z. Li, X. Luo and Y. Li, *ACS Omega*, 2022, **7**, 43829–43838.
63 A. Alkhouzaam and H. Qiblawey, *J. Membr. Sci.*, 2021, **620**, 118900.
64 J. Sharma, S. Sharma, U. Bhatt and V. Soni, *J. Hazard. Mater. Lett.*, 2022, **3**, 100069.
65 S. Takkar, B. Tyagi, N. Kumar, T. Kumari, K. Iqbal, A. Varma, I. S. Thakur and A. Mishra, *Environ. Technol. Innovation*, 2022, **26**, 102348.